A mild one-step method for enhancing optical absorption of amine-functionalized metal-organic frameworks

Shan Gao[a,b,1], Wanglai Cen[c,1], Qian Li[a], Jieyuan Li[c], Yunfeng Lu[d,**], Haiqiang Wang[a,b,*], Zhongbiao Wu[a,b]

[a] Key Laboratory of Environment Remediation and Ecological Health, Ministry of Education, College of Environmental & Resources Science, Zhejiang University, Hangzhou, 310058, PR China
[b] Zhejiang Provincial Engineering Research Center of Industrial Boiler & Furnace Flue Gas Pollution Control, Hangzhou, 310027, PR China
[c] Institute of New Energy and Low Carbon Technology, College of Architecture and Environment, Sichuan University, Chengdu, 610065, PR China
[d] Department of Chemical and Biomolecular Engineering, University of California Los Angeles, CA, 90095, USA

ARTICLE INFO

ABSTRACT

Metal-organic frameworks (MOFs) are of significant interest for photocatalysis using visible light. Here we discuss HOMO/LUMO gap modification of amine-functionalized MOFs through a mild one-step method. DFT calculation reveals the formation of covalent bond between TiO_2 and the amine from NH_2-MIL-125, narrowing the HOMO/LUMO gap of NH_2-MIL-125 by raising its HOMO level. After CdS quantum dots (QDs) deposited on this MOF@TiO_2 core-shell structure, this composite catalyst can act as an efficient visible-light-driven catalyst for NO removal. The integral coating of amorphous TiO_2 onto MOF octahedrons constructs a mesoporous protection shell upon MOF frameworks, providing a superior accommodation for embedding CdS QDs. Integrating MOF with TiO_2 also reduces undesirable electron-hole recombination by facilitating charge transfer to amorphous TiO_2. Possible mechanism of photocatalytic oxidation of NO over CdS/NH_2-MIL-125@TiO_2 catalysts is proposed. This work illustrates the possibility of tuning the optical response of NH_2-MOFs under very mild condition, and demonstrates the potential usage of MOF-based heterostructured photocatalysts.

1. Introduction

Metal-organic frameworks (MOFs) have attracted much attention recently and have been extensively studied in potential applications such as catalysis, photocatalysis, gas storage/separation, and molecular sensing [1,2]. When used in photocatalysis, MOFs can: (a) act as porous carriers for photocatalytically active species because of their porosity and large internal surface areas; (b) Or participate in the charge transfer process where their organic linkers can be used as light-harvesting units and photoexcited electrons can be transferred to inorganic clusters [3]. A couple of amine-functionalized MOFs have been reported to be photoactive under visible light irradiation. Fu *et al.* [4] reported a Ti-containing MOF, NH_2-MIL-125 as an efficient photocatalyst, which converts CO_2 to $HCOO^-$. UiO-66(Zr) has a very similar topology and d^0 metal-based clusters with MIL-125[3], and NH_2-UiO-66(Zr) also shows its photocatalytic activity under visible light [5,6]. NH_2-MIL-68(In) with a HOMO/LUMO gap of 2.82 eV was also proved to perform as an

efficient visible-light-driven photocatalyst with considerable activity and stability for the reduction of Cr(VI) [7].

One possible way to boost the photocatalytic efficiency is to tune the optical absorption of MOFs by modifying the aromatic ring of the linker. It has been demonstrated that the HOMO/LUMO gap energy of MOFs can be tuned by changing the organic linker [8]. When NH_2-MIL-125(Ti) was post-synthetically functionalized with dye-like molecular fragments, its HOMO/LUMO gap energy decreased by 0.53 eV theoretically, and it absorbs 100% more light in the visible region than NH_2-MIL-125(Ti) [9]. The modification of MIL-125 (Ti) with diaminated linker bdc-$(NH_2)_2$ also responds an enhanced adsorption in visible light [10]. It is confirmed that electronic modifications of the aromatic motifs directly control the optical properties through modification of the valence band.

Functionally integrating MOFs with an inorganic semiconductor facilitates electron transfer between the semiconductor and MOF [11], therefore is one of the best ways to promote MOF activity as a

photocatalyst. Wang et al. [1] coupled UiO-66 and g-C$_3$N$_4$ as a new hybrid photocatalyst for solar hydrogen production. Li and co-workers [11] synthesized Cu$_3$(BTC)$_2$@TiO$_2$ core-shell photocatalysts, and demonstrated that the charge transfer between MOFs and inorganic semiconductors suppresses the recombination of electron-hole in the semiconductors. Amorphous TiO$_2$ can be an excellent material in a hybrid composite owing to their porous properties. Growing amorphous TiO$_2$ layers on catalyst particles is a promising way to enhance photocatalytic activity and also to stabilize nanocrystals [12,13].

Quantum dots (QDs) of semiconductors have been attached to photocatalysts, such as CdS [14,15], CdSe [16], CdTe [17], PbS [18,19], and CuInS$_2$ [20], to enhance the photoactivity in visible light. CdS is a widely-used photocatalyst for visible-light-driven applications, and has a band gap (ca. 2.4 eV) that matches well with the relevant spectrum of sunlight [21]. CdS QDs embedded in mesoporous TiO$_2$ effectively extend the photoresponse of TiO$_2$ to the visible-light region and enhance the photocatalytic performance for NO oxidation [22]. CdS QDs sensitized Zn$_{1-x}$Cd$_x$S solid solutions also show improved photocatalytic activity for H$_2$ production due to the quantum size effect of CdS QDs [23]. Ge et al. [14] demonstrated the synergic effect of g-C$_3$N$_4$ coupled with CdS QDs and the efficient separation of the photogenerated charge carriers was revealed after the loading of CdS QDs.

In this paper, we proposed a mild one-step modification method to extend visible light absorption of amine-functionalized MOFs. It is realized by coating a thin layer of amorphous TiO$_2$ onto amine-functionalized MOFs under mild condition. Optical adsorption is enhanced due to the modification of NH$_2$ linkers by TiO$_2$. Coupled with highly dispersed CdS QDs, an efficient and visible-light-driven photocatalyst, CdS/NH$_2$-MIL-125@TiO$_2$ core-shell composite was developed for the first time. The as-synthesized photocatalyst shows improved visible-light photocatalytic performance and highly enhanced stability for NO removal at ambient temperature. The photocatalyst morphology, electronic structure, physical properties, and visible-light induced photocatalytic activities of these MOF-based catalysts were explored, and density functional theory (DFT) was applied. This methodology can be further extended to other MOFs with amine-linkers, which should enable HOMO/LUMO gap control under mild condition.

2. Materials and methods

2.1. Synthesis of NH$_2$-MIL-125(Ti)

NH$_2$-MIL-125(Ti) was synthesized according to a method reported in literature [4]. 6 mmol of 2-aminoterephthalic acid (H$_2$ATA) and 1.5 mmol of tetrabutyl titanate were dissolved in a solution containing 18 ml of N,N-Dimethylformamide (DMF) and 2 ml of methanol. The resulting mixture was stirred for 30 min at room temperature, and then transferred to a 100 ml Teflon liner and heated at 150 °C for 72 h. After cooling down to room temperature, the resultant suspension was filtered by centrifugation, then washed with DMF and with methanol afterwards. The light yellow product was vacuum dried at 80 °C to remove methanol from the pores.

2.2. Synthesis of NH$_2$-MIL-125@TiO$_2$

200 mg of NH$_2$-MIL-125 was dispersed in 100 ml of HCl (0.1 M). 3.275 ml of titanium(IV) bis(ammonium lactato)dihydroxide (TALH) (50 wt% solution in water) was added afterwards. Resulting dispersion was stirred at room temperature for 2 h. Then the coated particles were washed with water three times and isolated by centrifugation.

2.3. CdS quantum dots (QDs) deposition on MOFs

NH$_2$-MIL-125@TiO$_2$ or NH$_2$-MIL-125 samples were sequentially immersed in four different solutions or deionization water for 10 min during sonication, and isolated by centrifugation. The immersion order

follows: 0.025 M cadmium chloride (CdCl$_2$), deionization water, 0.025 M sodium sulfide (Na$_2$S), and deionization water. Such an immersion cycle was repeated for 5 times. The as-prepared samples were dried in a N$_2$ stream, and the samples were designated as CdS/NH$_2$-MIL-125@TiO$_2$ or CdS/NH$_2$-MIL-125.

2.4. Characterizations

The morphologies were observed by a Hitachi SU8010 SEM (Japan) and a JEOL JEM-2010 TEM (Japan). Nitrogen adsorption/desorption studies were conducted on a static adsorption instrument (JW-BK 132F, Beijing JWGB Sci & Tech Co., China). The pore size distribution was calculated by BJH desorption method. UV–vis absorption spectra were recorded on a Shimadzu UV-2450 spectrophotometer (Japan) in a spectral range of 200–800 nm. The photoluminescence spectra (PL) were obtained on a FLUOROLOG-3-TAU fluorometer (Jobin Yvon, Fance), using 380 nm laser as an excitation source. Transient photocurrent was measured on a 660E electrochemical analyzer (CH Instruments) in a standard three-electrode system with the as-prepared samples as the working electrodes having an active area of 1.0 cm^2, a platinum wire as the counter electrode, and Ag/AgCl (saturated KCl) as a reference electrode. 0.1 M Na$_2$SO$_4$ aqueous solution was used as the electrolyte. A xenon lamp (75 W) with a UV cut filter was utilized as the visible light source. Electron spin resonance (ESR) signals of spin-trapped paramagnetic species with 5,5-dimethyl-1-pyrroline N-oxide (DMPO) were recorded with an Edinburgh Instruments' Spectrometer (FLSP920, England). A 300 W Xe lamp (PLS-SXE 300, Beijing Perfectlight Co. Ltd) with a UV cutoff filter (λ > 420 nm) was used as a visible light irradiation source. The crystal structure of samples were analyzed by powder X-ray diffraction (PXRD) on a D/max RA X-ray diffractometer (Rigaku Co., Japan) with Cu Kα radiation. X-ray photoelectron spectroscopy (XPS) was recorded on Thermo ESCALAB 250 spectrometer (USA) with Al Kα radiation (hν = 1486.6 eV). The shift of the binding energy was corrected with respect to C 1 s (284.8 eV).

2.5. Visible light photocatalytic removal of NO

The photocatalytic removal of NO was performed at an ambient temperature in a continuous flow setup equipped with an online NO-NO$_2$-NO$_x$ analyzer (Thermo Scientific, Model 42i-TL, USA). The rectangular reactor (30 × 15 × 10 cm) was made of stainless steel and was cover with Saint-Gobain Glass, allowing the transmission of visible light. A 150 W tungsten halogen lamp was used as the light source for the photocatalytic reaction, equipped with a UV cut filter to cut off lights with wavelength < 420 nm. The as-prepared sample (0.20 g) was dispersed in deionization water (ca. 50 ml) under ultrasonic treatment for 10 min, and then uniformly coated onto two glass dishes (12.0 cm in diameter) when water was evaporated at 40 °C. After adsorbing NO at 0.05 V to saturation coverage, the lamp was turned on as the source of visible light. The NO conversion was defined as follow:

$$\text{NO conversion}(\%) = \frac{C_0 - C}{C_0} \times 100\%$$

where C$_0$ is the initial balanced concentration of NO and C is the concentration of NO at a given time in photocatalytic reaction process.

2.6. DFT calculations

All the spin polarized DFT-D2 calculations were carried out with the code VASP 5.3.5, [24] applying a generalized gradient approximation with the Perdew–Burke–Ernzerhof (PBE) exchange and correlation functional [25]. A plane-wave basis set with cut-off energy 400 eV within the framework of the projector-augmented wave method was utilized [26,27]. The Gaussian smearing width was set to 0.2 eV. The Brillouin zone was sampled with a 3 × 3 × 1 Monkhorst Pack grid. All atoms were relaxed and converged to 0.01 eV Å^{-1}. A 2 × 2 × 3
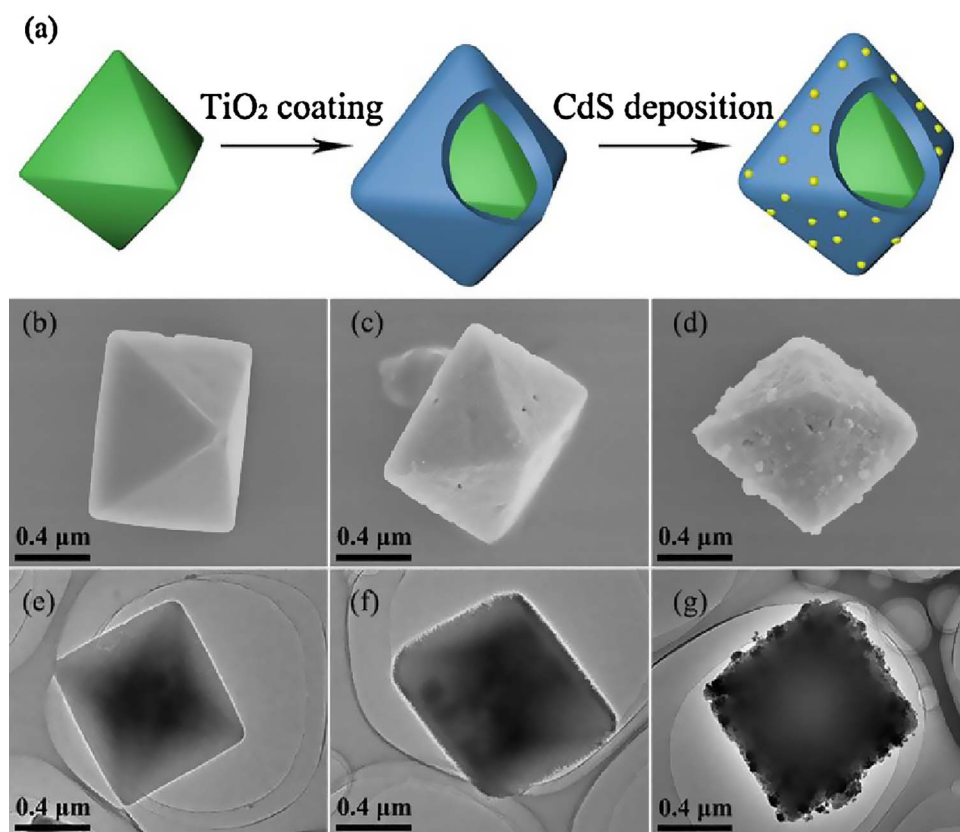
supercell of TiO$_2$ was relaxed as initial model, with a vacuum region of 10 Å.

The adsorption energy (ΔE_{ads}) is defined as

$$\Delta E_{ads} = E_{tot} - (E_{mol} + E_{TiO_2}) \tag{1}$$

where E_{tot}, E_{mol} and E_{TiO_2} are the total energy of the adsorption complex, the isolated MOF molecule and the pristine TiO$_2$, respectively.

3. Results and discussion

Fig. 1a is a schematic illustration of TiO$_2$ coatings on NH$_2$-MIL-125 crystals and CdS QDs embedding on core-shell NH$_2$-MIL-125@TiO$_2$. Octahedral NH$_2$-MIL-125 was prepared by solvothermal synthesis [4]. Scanning electron microscope (SEM) and Transmission electron microscope (TEM) observations indicated that pristine NH$_2$-MIL-125 consists of well-shaped octahedral crystals with clean and smooth surfaces (Fig. 1b, e). Powder X-ray diffraction (PXRD) patterns of as-synthesized NH$_2$-MIL-125 is identical to those of NH$_2$-MIL-125 samples reported in the literature (Fig. S1) [28,29].

To obtain NH$_2$-MIL-125@TiO$_2$ core-shell structure, a coating strategy was employed consisting of TALH (TiO$_2$ precursor) undergoing hydrolysis and condensation at room temperature [30,31]. After TiO$_2$ coating process, the surface of NH$_2$-MIL-125 becomes rough and grainy (Fig. 1c, f), but the octahedral profile is still inherited as core-shell structures. X-ray photoelectron spectroscopy (XPS) was conducted to determine the surface composition of samples (Table S1). After TiO$_2$ coating, the surface concentrations of C, N decreased, while those of Ti, O increased, indicating the coverage of TiO$_2$ shell upon NH$_2$-MIL-125. Elemental C and N (due to NH$_2$-MIL-125 inside TiO$_2$ shell) are clearly detected for NH$_2$-MIL-125@TiO$_2$ and CdS/NH$_2$-MIL-125@TiO$_2$. Considering that the detection depth of XPS with an Al target only reaches 3–10 nm [32–34], the thickness of the thin TiO$_2$ layer should be less than 10 nm. PXRD analysis (Fig. S1) confirms the unchanged crystal structure of NH$_2$-MIL-125 after TiO$_2$ coating. In addition, the good

agreement between the PXRD patterns of NH$_2$-MIL-125 and NH$_2$-MIL-125@TiO$_2$ (with no diffraction peak for TiO$_2$) indicates the amorphous nature of the TiO$_2$ shell.

CdS QDs were assembled onto the surface NH$_2$-MIL-125@TiO$_2$ structure by the sequential chemical bath deposition (S-CBD) method [22]. It can be seen in Fig. 1d and g that CdS QDs are supported on the surface of NH$_2$-MIL-125@TiO$_2$. An elemental map is shown in Fig. S2, in which blue, green, cyan, yellow, red, and orange areas represent Cd, S, Ti, O, C, and N distribution, respectively. It virtually indicates that CdS QDs were uniformly distributed over NH$_2$-MIL-125@TiO$_2$. PXRD patterns of CdS/NH$_2$-MIL-125@TiO$_2$ show a newly-appeared diffraction peak at 24.4°, belonging to the hexagonal structure of CdS [35]. It should be pointed out that the characteristic peak is rather weak due to the ultrasmall diameter of the CdS QDs. The quantitative analysis of XPS results (Table S1) reveals the molar ratio of Cd to S close to 1:1, confirming the stoichiometric formation of CdS.

NH$_2$-MIL-125 has a large surface area (1128.8 m^2/g, see Fig. 2a) and a large ratio of micropores with a homogeneous micropore size distribution (1060.9 m^2/g, see Fig. S3). The micropore size (D < 2 nm) distribution was obtained by Horvath-Kawazoe (HK) method, showing NH$_2$-MIL-125 has a narrow micropore size distribution with range of 0.50–0.59 nm and maxima at 0.51 and 0.56 nm (see Fig. S3). After amorphous TiO$_2$ coated on NH$_2$-MIL-125, the BET surface area increased from 1128.8 m^2/g to 1415.2 m^2/g (Fig. 2a), the micro- and mesoporous nature of MOFs are still obtained after TiO$_2$ coating (Fig. S3, S4). It is also noteworthy that the nitrogen adsorption-desorption isotherms of NH$_2$-MIL-125@TiO$_2$ present pronounced hysteresis loops, while the hysteresis is not so obvious in the isotherms of the pristine NH$_2$-MIL-125 sample. This reveals the formation of new mesopores upon the MOF structure after TiO$_2$ coating. The desorption branches were used to calculate the pore size distribution using the Barrett-Joyner-Halenda (BJH) methods (shown in Fig. S4). A narrow pore size distribution at around 2.5 nm was observed for the NH$_2$-MIL-125@TiO$_2$ sample, verifying that mesopores were constructed upon NH$_2$-MIL-125.
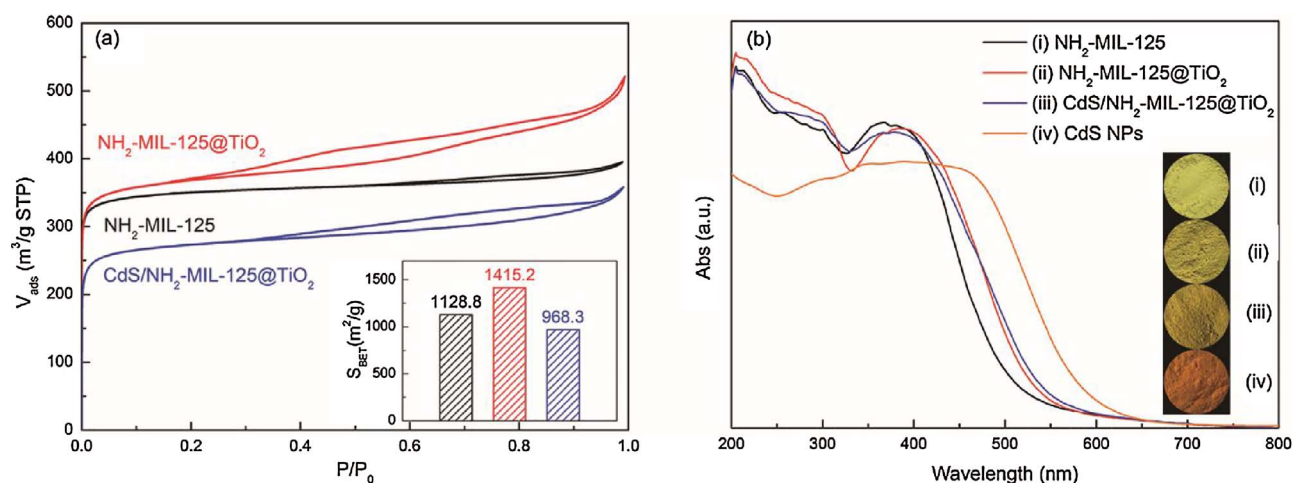
Fig. 2. (a) Nitrogen adsorption-desorption isotherms and Brunauer-Emmett-Teller (BET) surface area (bottom right) of NH_2-MIL-125 (black), NH_2-MIL-125@TiO_2 (red), and CdS/NH_2-MIL-125@TiO_2 (blue). (b) UV–vis adsorption spectra of NH_2-MIL-125, NH_2-MIL-125@TiO_2, CdS/NH_2-MIL-125@TiO_2 and CdS NPs. The inset shows corresponding colors of these samples. (For interpretation of the references to colour in this figure legend, the reader is referred to the web version of this article.)

This demonstrated that an amorphous TiO_2 shell could enrich mesopores on MOF frameworks, and result in a high surface area for the MOF samples. Although the deposition of CdS QDs decreases the surface area and blocks some of the micro- and mesopores, the CdS/NH_2-MIL-125@TiO_2 photocatalyst still maintains a large surface area (968.3 m^2/g) and porous structure.

UV–vis diffuse reflectance spectroscopy (DRS) was used to characterize the electronic states of the as-prepared samples. Fig. 2b compares the UV–vis absorbance of NH_2-MIL-125, NH_2-MIL-125@TiO_2, CdS/NH_2-MIL-125@TiO_2, CdS nanoparticles (NPs), and their corresponding colors. The spectrum of NH_2-MIL-125 shows two absorption edges near ca. 330 nm and 550 nm, corresponding to the absorption of Ti-O oxo-clusters and ligand-based absorption, respectively [10,29]. In comparison to the spectrum for pristine MOF, that of NH_2-MIL-125@TiO_2 shows a slight shift towards higher wavelengths and reaches further out in the visible region. Although TiO_2 itself can only excited by UV-irradiation with no adsorption in visible region, the amorphous TiO_2 shell unexpectedly results in an absorption edge red-shift of NH_2-MIL-125 (color changes from light yellow to darker yellow). CdS QDs/NH_2-MIL-125@TiO_2 catalyst shares a similar UV–vis spectrum with NH_2-MIL-125@TiO_2. Above all, the strong ability to absorb visible-light makes CdS/NH_2-MIL-125@TiO_2 a promising photocatalyst for solar-driven applications.

A Tauc plot was used in order to calculate the HOMO/LUMO gaps of the solids (Fig. S5). The HOMO/LUMO gaps for as-prepared NH_2-MIL-125 and NH_2-MIL-125@TiO_2 were determined to be 2.64 eV and 2.50 eV, respectively. This result suggests NH_2-MIL-125@TiO_2 is not a simple mixture of NH_2-MIL-125 and TiO_2, and the interaction between MOF and TiO_2 shell has influenced the HOMO/LUMO energies of the NH_2-MIL-125 frameworks.

This HOMO/LUMO gap decreasing method can be further extended to other NH_2-modified MOFs. The HOMO/LUMO gaps of pristine NH_2-MIL-125(Ti), NH_2-UIO-66(Zr), NH_2-MIL-68(In) and NH_2-MIL-101(Al) are determined to be 2.64 eV, 2.80 eV, 2.81 eV, and 2.80 eV, respectively (Fig. 3). After these MOFs were coated by a thin layer of TiO_2, their HOMO/LUMO gaps all decreased to 2.50 eV, 2.72 eV, 2.69 eV, and 2.73 eV, respectively. In comparison, no decreasing effects are observed on MIL-125(Ti) sample, whose HOMO/LUMO gap remains to be 3.26 eV before/after TiO_2 coating. This result poses some potential for HOMO/LUMO gap tuning of similar NH_2-modified MOFs.

To clarify the interaction between the NH_2-MOFs and TiO_2 shell, the XPS spectra for N 1 s of NH_2-MIL-125 and NH_2-MIL-125@TiO_2 were fitted (Fig. S6). The N 1 s spectra of pure NH_2-MIL-125 can be deconvoluted into three peaks at 399.5 eV, 400.9 eV, and 402.9 eV, assigned

to amine functionality stretching out of the MOF cavities, residual DMF in the framwork, and amine functionality protruding into the cavities. After NH_2-MIL-125 was covered by TiO_2, the peak at 402.9 eV negatively shifted to 402.2 eV. This provides strong evidence that the amine functionality stretching out of the MOF cavities interacted with TiO_2, thus altering the electronic and optical properties of NH_2-MIL-125.

In order to investigate the interaction between the MOF linkers and TiO_2, the electronic structure calculations on the MOF unit adsorbed on TiO_2 was performed using density functional theory (DFT). Fig. 4a shows a simplified model of the MOF binding unit that was used for computational calculations. The interaction of the MOF binding unit and TiO_2 and their charge density is depicted in Fig. 4b, and the density of states (DOS) curves are shown in Fig. 4c. DFT calculations show that the MOF unit was adsorbed onto TiO_2 with an adsorption energy of −0.45 eV. A weak covalent bond was formed between the N from the MOF linker unit and the Ti from TiO_2, and the N-Ti bond length turned out to be 2.38 Å. As shown in Fig. 4c, after the MOF unit was adsorbed onto the TiO_2 slab, the overall energies of N and C states becomes higher, approaching the Fermi level (0 eV), which is in accordance with the XPS results. The computational calculation and experimental results provide indirect evidence that the HOMO energy of NH_2-MIL-125 is probably increased to a higher energy occupied state.

Based on the computational study by Walsh [10], the LUMO of MIL-125(Ti) is primarily localized at the inorganic secondary building unit (Ti-oxocluster), increasing the amine content of the aromatic system of the linkers will not change the energy level. Therefore it is logical to assume that the interaction between the amine of the linkers and TiO_2 changes the HOMO energy whereas the LUMO energy remains nearly constant, narrowing the HOMO/LUMO gap of NH_2-MIL-125.

NO is chosen as a representative air pollutant to evaluate the performance of as-prepared photocatalysts. Fig. 5a compares the relative variations of NO removal rate against irradiation time for the samples. The adsorption/desorption equilibrium was attained before turning on the light. The activity of NH_2-MIL-125 reached a stable value of 30.9% after approximate 5 min. NH_2-MIL-125@TiO_2 exhibited a slightly boosted activity of 32.8%. After CdS QDs were deposited, CdS/NH_2-MIL-125@TiO_2 showed an enhanced activity of 48.4%, which is much higher than the CdS/NH_2-MIL-125 catalyst (38.6%).

To clarify whether the core-shell synergistic effect is exclusive to CdS/NH_2-MIL-125@TiO_2, several photocatalysts (with/without TiO_2 shell) were prepared and their photoactivity for NO removal was compared (Fig. S7). The NO conversion was improved markedly by the coating of amorphous TiO_2 for CdS, Pt, Pd deposited-, or bare MOF samples, proving that designing a core-shell structure by TiO_2 coating is
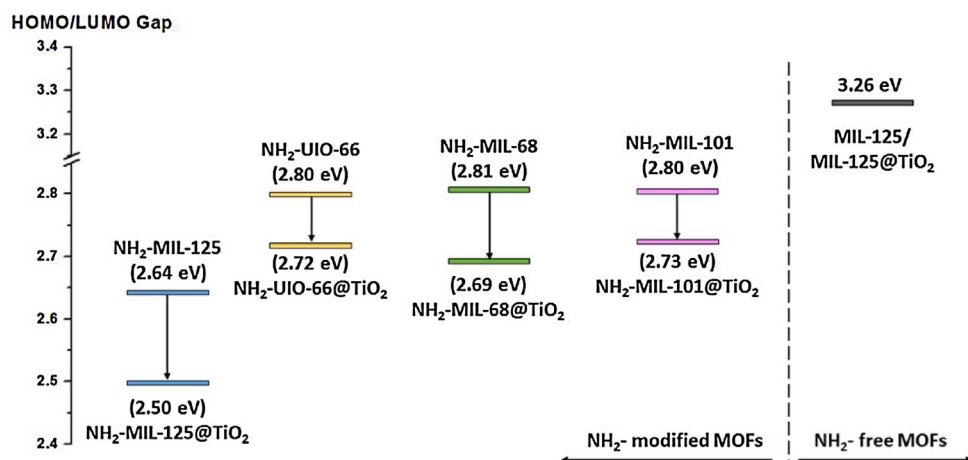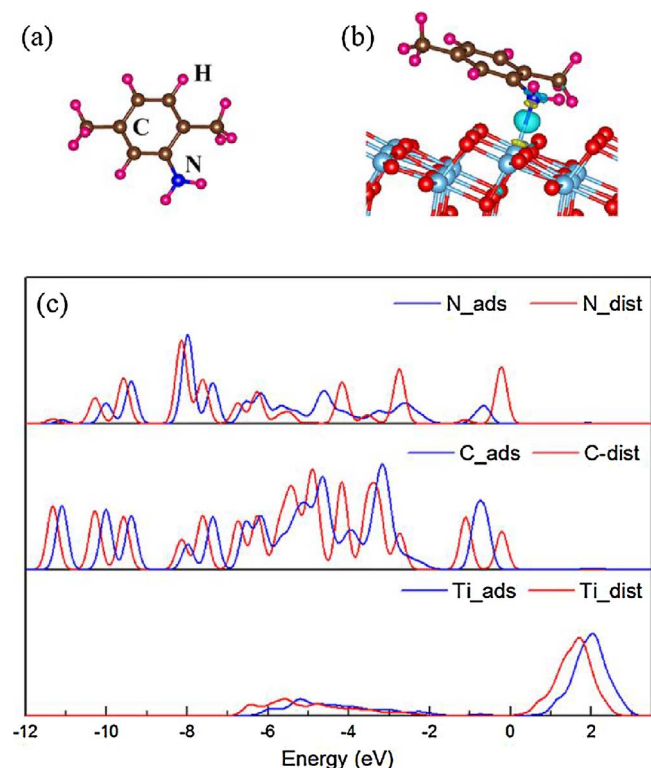
HOMO/LUMO Gap

Fig. 4. (a) Organic binding unit of MOF segment that used for DFT calculation; (b) Charge density for the adsorption of the MOF unit on TiO_2 slab; (c) Density of states of N, Ti and all the C atoms. Both the N and Ti are concerned during the adsorption in (b). Red for DOS curves when MOF unit was distant from TiO_2 slab, Blue for DOS curves when MOF unit was adsorbed onto TiO_2 slab. (For interpretation of the references to colour in this figure legend, the reader is referred to the web version of this article.)

an universal method to improve the photoactivity of NH_2-MIL-125. UV–vis spectra and PL spectra have demonstrated the advantage of the TiO_2 shell by enhancing the light harvesting ability and reducing the photoelectron-hole recombination rate. Sooho Lee et al. [12] also reported that a thin shell of amorphous TiO_2 served as a channel for charge carriers, and enhanced photocatalytic hydrogen production by forming a staggered band offset with CdSe nanocrystals.

The visible photocatalytic reaction for NO removal involves the oxidation of NO to HNO_2 and/or HNO_3 [36,37], and the accumulation of HNO_2 and HNO_3 on the catalyst surface would result in deactivation of some photocatalysts [38,39]. In this study, the TiO_2 shell coated upon the MOF crystals is proposed to protect catalysts from corrosion and/or poisoning by nitrates and nitrites in a photocatalytic reaction.

To verify this hypothesis, the long-term stability of photocatalytic activity was tested when the inlet concentration of NO was increased to 100 times (Fig. 5b). CdS deposited on NH_2-MIL-125@TiO_2 core-shell structure has a much stronger capacity for NO_x removal in a long term test than that deposited on bare NH_2-MIL-125, suggesting that TiO_2 coating could act as a shield to protect the MOF catalyst from corrosion and/or poisoning. Similar thoughts have also been reported by other authors. Shu Hu et al. [13] reported that amorphous TiO_2 grown on Si, GaAs, and GaP photoanodes could prevent corrosion, had electronic defects that promote hole conduction, and were sufficiently "transparent" to reach the light-limited performance of protected semiconductors. The repeated visible light photocatalytic activity of CdS/ NH_2-MIL-125@TiO_2 catalyst was also tested (Fig. S8). No distinct activity decay is observed after five recycling runs, indicating the photochemical stability and durability under repeated irradiation.

Fig. S9 compares the morphology of CdS embedded on core-shell MOF@TiO_2 structure or on bare MOF. On bare NH_2-MIL-125 crystals, CdS particles tend to aggregate together randomly (TEM images in Fig. S9a), resulting in a relatively poor dispersion. In contrast, CdS has a much better distribution upon the NH_2-MIL-125@TiO_2 core-shell structure (Fig. S9b). This result could probably be explained by the hydrophilic and microporous properties of amorphous TiO_2, where Cd^{2+} and S^{2-} ions could diffuse and penetrate into the micropores of TiO_2. Therefore amorphous TiO_2 shell on NH_2-MIL-125 has a tighter attachment with CdS, and provides a superior accommodation for embedding CdS QDs.

The high-resolution TEM (HRTEM) image of CdS/NH_2-MIL-125@TiO_2 photocatalyst is illustrated in Fig. S9c, which shows several CdS QDs growing on the surface of NH_2-MIL-125@TiO_2 (dot ellipses). The average diameter of CdS QDs was about 4.5 nm, with sizes ranging from ca. 5 to 11 nm (insert, Fig. S9c). The lattice spacing of 0.314 nm displayed in Fig. S9c corresponds to the (101) plane of CdS (JCPDS: 41–1049).

To investigate the charge separation properties of the CdS/NH_2-MIL-125@TiO_2 composites, the samples were characterized using steady-state photoluminescence (PL) spectroscopy. The PL spectra are showed in Fig. 6a. NH_2-MIL-125 shows a significant PL emission peak centered at ca. 450 nm. Compared with pure NH_2-MIL-125, the PL emission is strongly quenched when NH_2-MIL-125 is coated by amorphous TiO_2. This indicates the efficient electron transfer from the LUMO of NH_2-MIL-125 to the conduction band of amorphous TiO_2, thereby retaining the holes in the valence band of NH_2-MIL-125. After CdS is deposited on the surface, the depression of PL emission becomes more noticeable.

The time-resolved photoluminescence (TRPL) spectra of catalysts are compared in Fig. 6b. These spectra were fitted using a biexponential function expressed as follows:
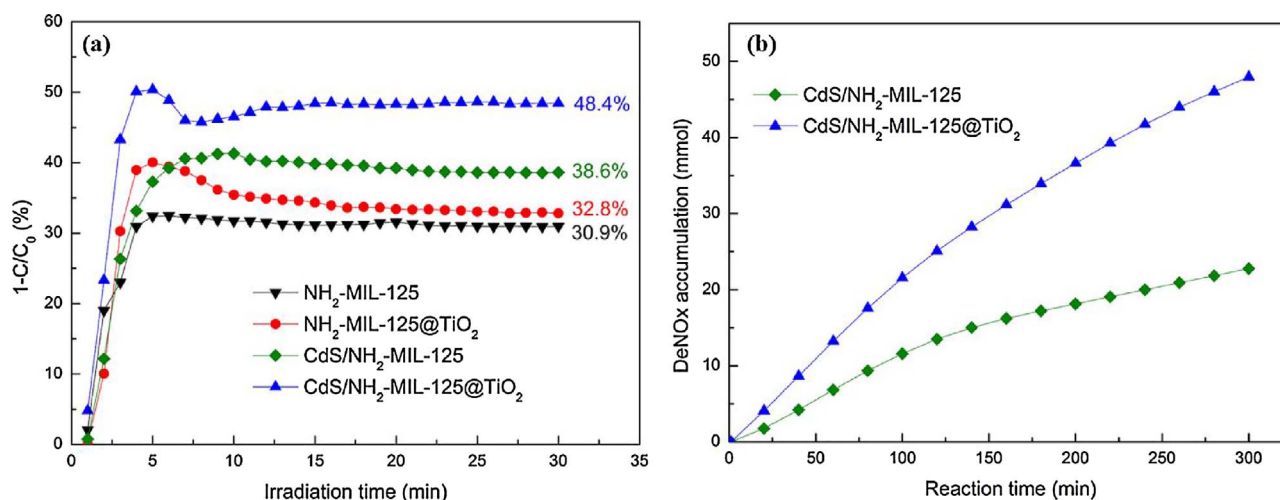
Fig. 5. (a) Photocatalytic activity of as-prepared photocatalysts for NO removal under visible light irradiation; (b) Long term accumulation of removed NO over two samples.

$$I(t) = A_1 \exp(-t/\tau_1) + A_2 \exp(-t/\tau_2)$$

where A_1 and A_2 are the amplitudes (or weighing factors), and τ_1 and τ_2 are the corresponding lifetimes.

The fitting results are summarized in the table inset in Fig. 6b, showing a short lifetime component (τ_1) and a long lifetime component (τ_2). For pristine NH_2-MIL-125, the short and long lifetimes are 1.0 ns and 7.3 ns, respectively. In the presence of the TiO_2 shell, the short and long lifetimes of NH_2-MIL-125@TiO_2 decrease to 0.5 ns and 5.0 ns, respectively. There is a clear quenching of both the lifetimes in the transients, indicating faster interfacial electron transfer [40]. The highly efficient charge transfer and charge separation at the NH_2-MIL-125@TiO_2 can contribute to a higher photocatalytic activity, as the charge recombination in NH_2-MIL-125 can be effectively inhibited. After the deposition of CdS QDs, the long lifetime of CdS/NH_2-MIL-125@TiO_2 decreases slightly to 4.7 ns while the short lifetime remains unchanged at 0.5 ns.

Fig. S10 provides the transient photocurrent responses of NH_2-MIL-125, NH_2-MIL-125@TiO_2, and CdS/NH_2-MIL-125@TiO_2 under intermittent visible light. The stable photocurrent value of NH_2-MIL-125@TiO_2 is about 7 times as high as that of bare NH_2-MIL-125, demonstrating that NH_2-MIL-125 coated by TiO_2 harvests visible light more efficiently than NH_2-MIL-125. Furthermore, CdS deposition also results in further enhancement of the photocurrent.

The electron spin resonance (ESR) spin-trap technique (with DMPO) was employed to probe the active oxygen species generated under visible light irradiation (Fig. 7). Neither the DMPO-·OH nor DMPO-·O_2^- spin adducts had been detected without irradiation. Under visible light irradiation, typical characteristic peaks of ESR signals for DMPO-·OH and DMPO-·O_2^- adducts were observed, confirming that ·OH and ·O_2^- radicals have been produced during the photocatalytic reaction. The signals of ·OH and ·O_2^- radicals for NH_2-MIL-125@TiO_2 are stronger than those of pristine NH_2-MIL-125, and the signals are further enhanced after CdS QDs were embedded on NH_2-MIL-125@TiO_2. These results suggest that TiO_2 coated and CdS embedded MOF catalyst could produce more radicals, which is responsible for its enhanced photocatalytic activity.

The Mott-Schottky plots of NH_2-MIL-125, amorphous TiO_2, and CdS are used to determine their flat-band potential (V_{fb}), and Tauc plots were used to calculate their "band gaps". The flat-band potential of NH_2-MIL-125, amorphous TiO_2, and CdS which were ca. −1.10, −0.50, −0.70 V vs. Ag/AgCl, respectively (Fig. S11a). When NHE is used as the standard, the LUMO potential of NH_2-MIL-125 is around −0.9 V, and the lowest conduction band (CB) potential of amorphous TiO_2, and CdS is −0.30 and −0.50, respectively. HOMO/LUMO gaps for as-prepared NH_2-MIL-125 was 2.28 eV, and the band gap of amorphous TiO_2 and CdS are estimated to be 3.25 and 2.64 eV, respectively (Fig. S11b).

Based on the Mott-Schottky plots and Tauc plots, the LUMO/HOMO or CB/VB energies are determined to be −0.90/+1.74 (for NH_2-MIL-125), −0.30/+2.98 (for amorphous TiO_2), −0.50/+1.78 (for CdS) vs.

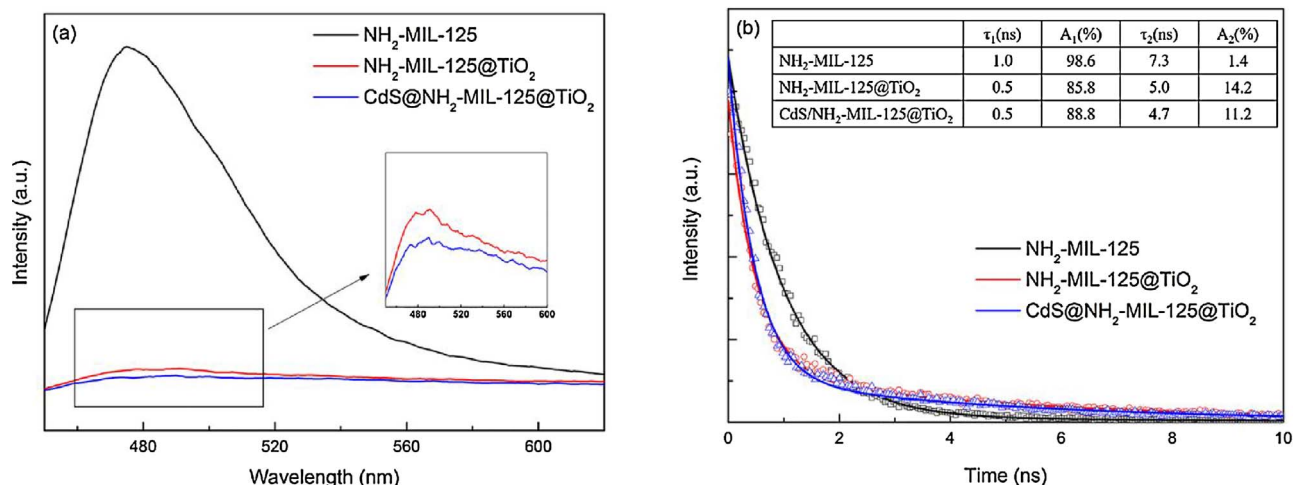**Fig. 6.** (a) The stable state PL spectra and (b) time-resolved PL spectra of NH_2-MIL-125, NH_2-MIL-125@TiO_2, and CdS/NH_2-MIL-125@TiO_2.

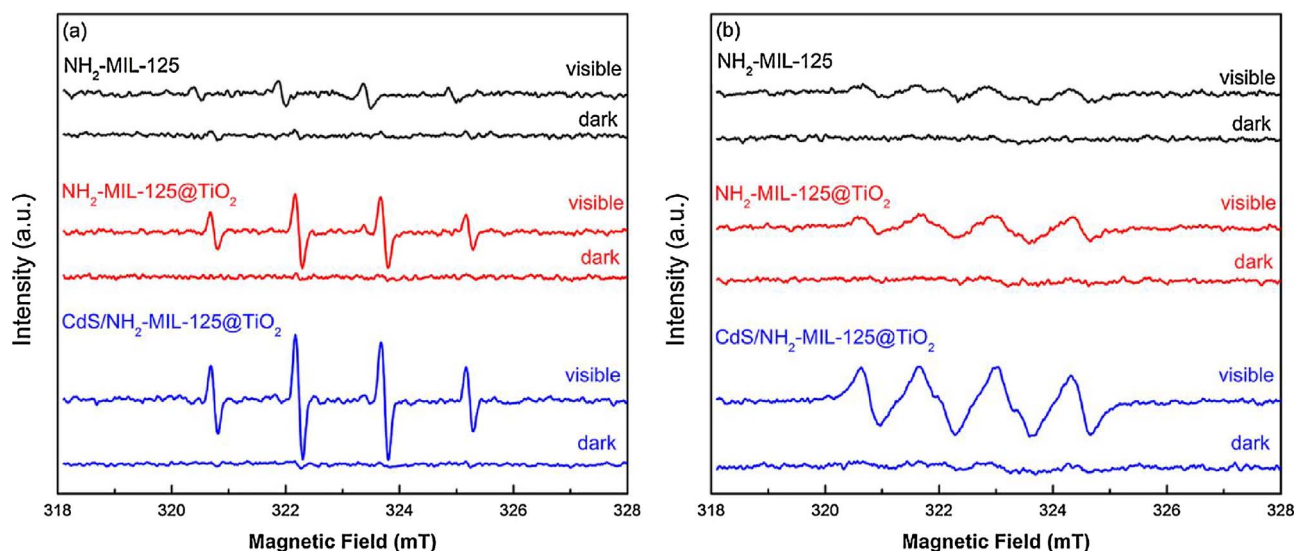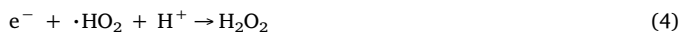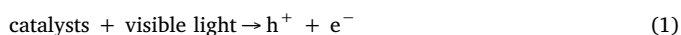|	τ_1(ns)	A_1(%)	τ_2(ns)	A_2(%)
NH_2-MIL-125	1.0	98.6	7.3	1.4
NH_2-MIL-125@TiO_2	0.5	85.8	5.0	14.2
CdS/NH_2-MIL-125@TiO_2	0.5	88.8	4.7	11.2

Fig. 7. DMPO spin-trapping ESR spectrum for (a) DMPO-·OH and (b) DMPO-·O_2^-.

NHE, respectively. The HOMO energy of NH_2-MIL-125 is increased to $+1.60$ V when the HOMO/LUMO gap is narrowed by 0.14 eV after the organic linker is bonded with TiO_2. The LUMO potential of MOF and the CB potential of TiO_2 and CdS are more negative than the potential for the reduction of oxygen ($O_2 \rightarrow \cdot O_2^-$, -0.28 V vs. NHE)[41,42], suggesting that electrons on NH_2-MIL-125, TiO_2, or CdS could theoretically react with O_2 to form $\cdot O_2^-$ (Eqs. (1) and (2) [36]). Additional, the ESR spectrum for DMPO-·O_2^- demonstrated the massive production of $\cdot O_2^-$ on the CdS/NH_2-MIL-125@TiO_2 catalyst.

Judging from the fact that the HOMO energy of NH_2-MIL-125 ($+1.74$ V) and the VB of CdS ($+1.78$ V) are lower than the potential energy of $OH^-/\cdot OH$ (1.99 eV vs. NHE[43,44]) and $H_2O/\cdot OH$ (2.27 eV vs. NHE[43]), it can be determined that they are not appropriate for the direct generation of $\cdot OH$ radicals from OH^- or H_2O. Therefore, the potential pathway for $\cdot OH$ generation over a photocatalyst is the transformation of $\cdot O_2^-$ (via $\cdot O_2^- \rightarrow H_2O_2 \rightarrow \cdot OH$ route, the quantitative analysis of H_2O_2 formation is shown in Fig. S12), following the photochemical processes as listed below[36,43,45]:

$$\text{catalysts} + \text{visible light} \rightarrow h^+ + e^- \tag{1}$$

$$e^- + O_2 \rightarrow \cdot O_2^- \tag{2}$$

$$\cdot O_2^- + H^+ \rightarrow \cdot HO_2 \tag{3}$$

$$e^- + \cdot HO_2 + H^+ \rightarrow H_2O_2 \tag{4}$$

$$H_2O_2 + e^- \rightarrow \cdot OH + OH^- \tag{5}$$

$$h+ + OH- \rightarrow \cdot OH \tag{6}$$

The oxidation reaction of NO could then be initiated by $\cdot OH$ and $\cdot O_2^-$ radicals as follows [36,38,45]:

$$NO + \cdot OH \rightarrow HNO_2 \tag{7}$$

$$HNO_2 + \cdot OH \rightarrow NO_2 + H_2O \tag{8}$$

$$NO_2 + \cdot OH \rightarrow HNO_3 \tag{9}$$

$$NO + \cdot O_2^- \rightarrow NO_3^- \tag{10}$$

On the basis of the above discussion, a probable mechanism for the NO removal is proposed, as illustrated in Scheme 1. Under visible light irradiation, NH_2-MIL-125 and CdS QDs are both photoexcited to generate charge carriers. The photogenerated electrons of NH_2-MIL-125 and CdS QDs can be quickly transferred to amorphous TiO_2 owing to their intimate interfacial contact and matched band positions. Therefore, the excited electron/hole pairs are separated effectively, which

contributes to the improvement of photoelectrochemical properties of CdS/NH_2-MIL-125@TiO_2. Oxygen reacts with electrons (and protons) to form $\cdot O_2^-$ and $\cdot OH$ and the produced radicals further oxidize NO to form HNO_2 and HNO_3. In the photocatalytic reaction, each component of the core-shell catalyst performs its own functions: NH_2-MIL-125 has remarkable surface area for adsorption and act as a visible-light-driven photocatalyst itself; QDs as a co-catalyst, has a well matched band gap with the relevant spectrum of sunlight, which favors the visible light adsorption and enhances photoactivity; TiO_2 shell performs like a buffer layer between NH_2-MIL-125 and CdS QDs, contributing to the separation of charge carriers and enhancement of the visible light adsorption.
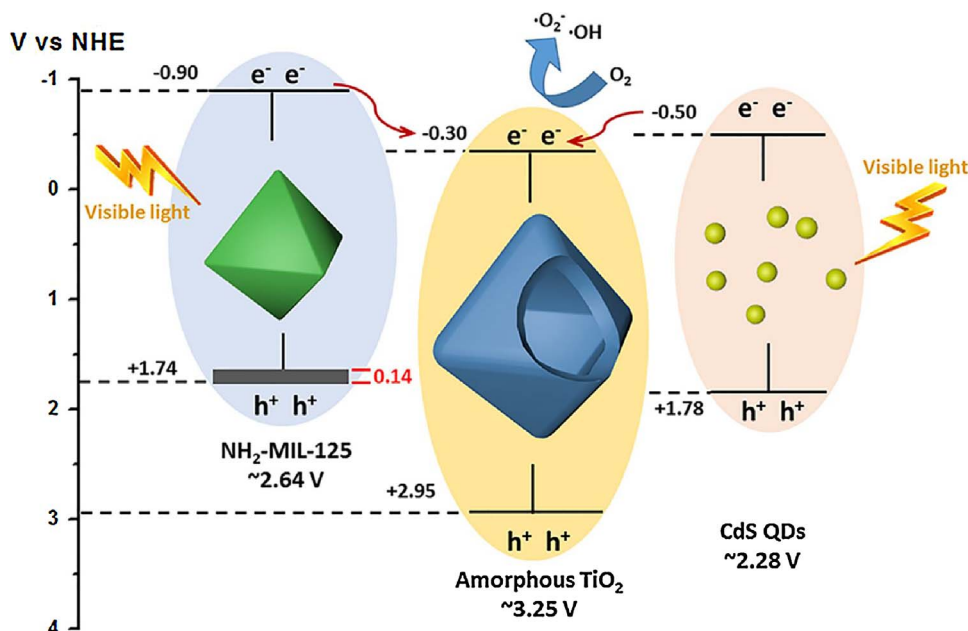
4. Conclusion

In this study, we proposed a one-step mild method for NH_2-MOFs to tune their HOMO/LUMO gaps. NH_2-MOFs coupled with a thin layer of TiO_2 in core-shell morphology can narrows the HOMO/LUMO gap of NH_2-MIL-125 by raising its HOMO energy, which promotes photoexcition under visible light. The thin TiO_2 shell also enhancing light harvest and suppresses undesirable electron-hole recombination, contrary to a prevailing notion that amorphous oxides are poor catalysts. CdS QDs embedded on core-shell NH_2-MIL-125@TiO_2 is a promising catalyst with visible light photocatalytic activity. It shows more stability in a long-term reaction for NO removal than that without TiO_2 shell. This HOMO/LUMO gap modification is universal for other NH_2-MOFs, thus pointing a potential way to tuning the HOMO/LUMO gaps through the mild one-step method proposed here.

Appendix A. Supplementary data

Supplementary data associated with this article can be found, in the online version, at https://doi.org/10.1016/j.apcatb.2018.01.007.

V vs NHE

−0.90   e⁻ e⁻

·O₂⁻ ·OH

O₂

−0.30   e⁻ e⁻   −0.50   e⁻ e⁻

Visible light

Visible light

+1.74   h⁺ h⁺   ⊏0.14

NH₂-MIL-125
~2.64 V

+2.95

+1.78   h⁺ h⁺

h⁺ h⁺

Amorphous TiO₂
~3.25 V

CdS QDs
~2.28 V

Scheme 1. Possible mechanism of photocatalytic oxidation of NO over CdS/NH₂-MIL-125@TiO₂ catalysts.

References

[1] R. Wang, L. Gu, J. Zhou, X. Liu, F. Teng, C. Li, Y. Shen, Y. Yuan, Adv. Mater. Interfaces 2 (2015) 1500037.
[2] M. Ranocchiari, J.A. van Bokhoven, PCCP 13 (2011) 6388–6396.
[3] M. Nasalevich, M. Van der Veen, F. Kapteijn, J. Gascon, CrystEngComm 16 (2014) 4919–4926.
[4] Y. Fu, D. Sun, Y. Chen, R. Huang, Z. Ding, X. Fu, Z. Li, Angew. Chem. 124 (2012) 3420–3423.
[5] C. Gomes Silva, I. Luz, F.X. Llabrés i Xamena, A. Corma, H. García, Chem. Eur. J. 16 (2010) 11133–11138.
[6] D. Sun, Y. Fu, W. Liu, L. Ye, D. Wang, L. Yang, X. Fu, Z. Li, Chem. Eur. J. 19 (2013) 14279–14285.
[7] R. Liang, L. Shen, F. Jing, W. Wu, N. Qin, R. Lin, L. Wu, Appl. Catal. B 162 (2015) 245–251.
[8] J. Gascon, M.D. Hernándezalonso, A.R. Almeida, G.P. van Klink, F. Kapteijn, G. Mul, Chemsuschem 1 (2008) 981–983.
[9] M.A. Nasalevich, M.G. Goesten, T.J. Savenije, F. Kapteijn, J. Gascon, Chem. Commun. 49 (2013) 10575–10577.
[10] C.H. Hendon, D. Tiana, M. Fontecave, C. Sanchez, L. D'arras, C. Sassoye, L. Rozes, C. Mellot-Draznieks, A. Walsh, J. Am. Chem. Soc. 135 (2013) 10942–10945.
[11] R. Li, J. Hu, M. Deng, H. Wang, X. Wang, Y. Hu, H.L. Jiang, J. Jiang, Q. Zhang, Y. Xie, Adv. Mater. 26 (2014) 4783–4788.
[12] S. Lee, K. Lee, W.D. Kim, S. Lee, D.J. Shin, D.C. Lee, J. Phys. Chem. C 118 (2014) 23627–23634.
[13] S. Hu, M.R. Shaner, J.A. Beardslee, M. Lichterman, B.S. Brunschwig, N.S. Lewis, Science 344 (2014) 1005–1009.
[14] L. Ge, F. Zuo, J. Liu, Q. Ma, C. Wang, D. Sun, L. Bartels, P. Feng, J. Phys. Chem. C 116 (2012) 13708–13714.
[15] S.W. Cao, Y.P. Yuan, J. Fang, M.M. Shahjamali, F.Y.C. Boey, J. Barber, S.C. Joachim Loo, C. Xue, Int. J. Hydrogen Energy 38 (2013) 1258–1266.
[16] C. Harris, P.V. Kamat, ACS Nano 4 (2010) 7321–7330.
[17] Y.S. Li, F.L. Jiang, Q. Xiao, R. Li, K. Li, M.F. Zhang, A.Q. Zhang, S.F. Sun, Y. Liu, Appl. Catal. B 101 (2010) 118–129.
[18] C. Ratanatawanate, Y. Tao, K.J. Balkus Jr., J. Phys. Chem. C 113 (2009) 10755–10760.
[19] C. Wang, R.L. Thompson, P. Ohodnicki, J. Baltrus, C. Matranga, J. Mater. Chem. 21 (2011) 13452–13457.
[20] F. Shen, W. Que, Y. Liao, X. Yin, Ind. Eng. Chem. Res. 50 (2011) 9131–9137.
[21] J. Yu, J. Jin, B. Cheng, M. Jaroniec, J. Mater. Chem. A 2 (2014) 3407–3416.
[22] W. Sun, Y. Yu, H. Pan, X. Gao, Q. Chen, L. Peng, J. Am. Chem. Soc. 130 (2008) 1124–1125.
[23] J. Yu, J. Zhang, M. Jaroniec, Green Chem. 12 (2010) 1611–1614.
[24] G. Kresse, J. Furthmüller, Matter Mater. Phys. 54 (1996) 11169–11186.
[25] J.P. Perdew, K. Burke, M. Ernzerhof, Phys. Rev. Lett. 77 (1996) 3865–3868.
[26] P.E. Blöchl, Phys. Rev. B 50 (1994) 17953–17979.
[27] G. Kresse, D. Joubert, Phys. Rev. B 59 (1999) 1758–1775.
[28] S.N. Kim, J. Kim, H.Y. Kim, H.Y. Cho, W.S. Ahn, Catal. Today 204 (2013) 85–93.
[29] D. Sun, L. Ye, Z. Li, Appl. Catal. B 164 (2015) 428–432.
[30] S.W. Lee, J. Drwiega, C.Y. Wu, D. Mazyck, W.M. Sigmund, Chem. Mater. 16 (2004) 1160–1164.
[31] K.E. DeKrafft, C. Wang, W. Lin, Adv. Mater. 24 (2012) 2014–2018.
[32] L.X. C. N. H. B. X. X. C. G. D. I. W. Y., Nanoscale 7 (2015) 14872-14880.
[33] M. Gao, S. Huang, L. Dai, G. Wallace, R. Gao, Z. Wang, Angew. Chem. 39 (2000) 3664–3667.
[34] T. Fukano, T. Motohiro, Sol. Energy Mater. Sol. Cells 82 (2004) 567–575.
[35] M. Pattabi, B.S. Amma, Sol. Energy Mater. Sol. Cells 90 (2006) 2377–2383.
[36] F. Dong, Z. Wang, Y. Li, W.K. Ho, S. Lee, Environ. Sci. Technol. 48 (2014) 10345–10353.
[37] F. Dong, Y. Sun, M. Fu, Z. Wu, S. Lee, J. Hazard. Mater. 219 (2012) 26–34.
[38] G.S. Li, D.Q. Zhang, J.C. Yu, Environ. Sci. Technol. 43 (2009) 7079–7085.
[39] C.H. Ao, S.C. Lee, Appl. Catal. B 44 (2003) 191–205.
[40] X. Wang, C. Liow, A. Bisht, X. Liu, T.C. Sum, X. Chen, S. Li, Adv. Mater. 27 (2015) 2207–2214.
[41] G. Xi, B. Yue, J. Cao, J. Ye, Chem. Eur. J. 17 (2011) 5145–5154.
[42] A. Fujishima, T.N. Rao, D.A. Tryk, J. Photochem. Photobiol. C 1 (2000) 1–21.
[43] Y. Cui, J. Huang, X. Fu, X. Wang, Catal. Sci. Technol. 2 (2012) 1396–1402.
[44] W. Liu, M. Wang, C. Xu, S. Chen, X. Fu, Mater. Res. Bull. 48 (2013) 106–113.
[45] X. Xiao, W. Zhang, J. Yu, Y. Sun, Y. Zhang, F. Dong, Catal. Sci. Technol. 6 (2016).